PHYSICAL REVIEW D **109,** 035003 (2024)

Hunting muonic forces at emulsion detectors

Akitaka Ariga,[1,2,*] Reuven Balkin,[3,†] Iftah Galon,[3,‡] Enrique Kajomovitz,[3,§] and Yotam Soreq[3,∥]
[1]*Albert Einstein Center for Fundamental Physics, Laboratory for High Energy Physics, University of Bern, Sidlerstrasse 5, CH-3012 Bern, Switzerland*
[2]*Department of Physics, Chiba University, 1-33 Yayoi-cho Inage-ku, 263-8522 Chiba, Japan*
[3]*Physics Department, Technion—Israel Institute of Technology, Haifa 3200003, Israel*

(Received 20 July 2023; accepted 2 January 2024; published 8 February 2024)

Only two types of Standard Model particles are able to propagate the 480meters separating the ATLAS interaction point and FASER: neutrinos and muons. Furthermore, muons are copiously produced in proton collisions. We propose to use FASERν as a muon fixed target experiment in order to search for new bosonic degrees of freedom coupled predominantly to muons. These muon force carriers are particularly interesting in light of the recent measurement of the muon anomalous magnetic moment. Using a novel analysis technique, we show that even in the current LHC run, FASERν could potentially probe previously unexplored parts of the parameter space. In the high-luminosity phase of the LHC, we find that the improved sensitivity of FASERν2 will probe unexplored parameter space and may be competitive with dedicated search proposals.

DOI: 10.1103/PhysRevD.109.035003

I. INTRODUCTION

The Standard Model of particle physics (SM) successfully describes Nature in a wide range of energy scales. However, there is experimental evidence and strong theoretical arguments for the existence of new physics (NP) beyond the SM (BSM), see, e.g., [1]. New feebly interacting particles (FIPs) at the MeV–to–GeV mass range are well-motivated in many BSM scenarios and have recently received a lot of attention, both on the theoretical and experimental side [2,3]. One particular subset of FIPs are bosons with nonuniversal couplings to the SM fermions, which appear in various extensions of the SM [4–7].

Bosons which couple predominantly to muons, referred to as muonic force carriers (MFCs), are motivated by the measurement of the muon anomalous magnetic moment, $(g-2)_\mu$ [8–10]. Comparing the experimental data to the data-driven SM prediction points to an anomaly, which can be explained by a weakly-coupled sub-GeV MFC, e.g., [11,12]. However, recent lattice results [13–15] seem to suggest the data is in fact consistent with the SM. Moreover, a recent measurement of the $e^+e^- \to \pi\pi$ cross section even appears to alleviate the tension between the data-driven SM prediction and the experimental result [16].

On the other hand, it is possible that NP contributions to $(g-2)_\mu$ are suppressed due to cancellation at the quantum level. This was demonstrated in [17], where an approximate cancellation at the 1-loop level arises due to a global symmetry. This type of scenario provides a clear motivation for more direct, tree-level searches, such as the one proposed here.

MFCs were targeted by direct searches in flavor factories [18,19] and NA62 [20,21], while vector MFCs were also probed by neutrino beam experiments [22–24]. In addition, there is a bound from supernova SN1987 [25,26]. Proposed experiments such as NA64$_\mu$ [5,27,28], M^3 [29] and beam dumps [30,31] can potentially probe unexplored regions of the MFC parameter space. An alternative approach is to maximize the NP reach of running experiments. For example, the ATLAS experiment can probe the MFC parameter space via missing momentum measurements [32].

In this work, we present a novel method to search for MFCs using emulsion detectors as muon fixed targets. In particular, we estimate the sensitivity of FASERν [33–35], the front part of the FASER experiment [36–39], to the MFC parameter space. The muons are produced in proton collisions, mostly as decay products or in secondary interactions between the collision products and the surrounding matter. Although most muons are deflected, an estimate of $N_\mu \sim 10^9$ muons with energy above 100 GeV are expected to reach FASERν with 150 fb^{-1} integrated

---

[*] akitaka.ariga@lhep.unibe.ch
[†] reuven.b@campus.technion.ac.il
[‡] iftah.galon@gmail.com
[§] enrique@physics.technion.ac.il
[∥] soreqy@physics.technion.ac.il

luminosity [39]. Using missing energy signatures, we estimate that MFC couplings as small as $10^{-3} - 10^{-4}$ may be within reach in FASERν and even smaller with FASERν2, which is expected to be installed at the LHC high luminosity (HL-LHC) stage. The sensitivity crucially depends on the background rejection efficiency, which must be carefully estimated in a dedicated detector study left for future work.

II. SIMPLIFIED MODEL

We consider a simplified model in which the muon is coupled to a light mediator $\chi = \{S, V\}$, with the Lagrangians,

$$\mathcal{L}_S = g_S S \bar{\mu}\mu, \qquad \mathcal{L}_V = g_V V_\alpha \bar{\mu}\gamma^\alpha \mu, \tag{1}$$

for a scalar and vector MFC, respectively, with the masses denoted by m_χ. Pseudoscalars and axial vectors are expected to give similar results. The effective theory described by Eq. (1) can emerge as a low energy limit of a UV complete theory; for example scalar interactions can arise as a result of integrating out heavy leptons [20], while the vector interactions naturally arise in a spontaneously broken gauged $U(1)_{L_\mu - L_\tau}$ theory [40–42].

Assuming χ is negligibly coupled to other SM constituents (e.g., the irreducible one-loop level coupling of S to photons), we consider the case where it is either long-lived at the detector scale or decays invisibly. This scenario can arise naturally in the muonphillic case when $m_\chi < 2m_\mu$, while above the dimuon threshold some more assumptions are required, e.g., sizable decay rate to a dark sector. Either way, once scattered against a fixed-target N, some muons lose a fraction of their energy due to the 2-to-3 process,

$$N + \mu \to N + \mu + \chi, \tag{2}$$

while χ or its dark sector decay products escape the system without depositing any energy in the detector. Thus, χ can be searched for using missing-momentum signatures in FASERν, utilizing it as a muon-fixed-target experiment.

III. METHOD

FASERν is an emulsion detector mounted in front of the FASER main detector. It is composed of 730 emulsion layers interleaved with 1.1 mm thick tungsten plates of area $S = 25\ \mathrm{cm} \times 30\ \mathrm{cm}$ [43]. As muons pass through FASERν, their track are measured by the emulsion layers. Throughout this work, we assume each layer provides only the position of the muon as it passes. In principle, due to the finite thickness of the emulsion layer and its structure, additional angular information can be deduced, which can potentially be harnessed to improve the analysis. We characterize each muon passing through FASERν by two simple properties: (i) the ratio between the final and the initial muon energies, $\mathcal{R}_{fi} \equiv (E_\mu)_f/(E_\mu)_i$, and (ii) the largest scattering angle of the track, θ_μ, which characterizes the largest kink in the track. Large kinks are strongly correlated with large energy losses. To fully benefit from the layered structure of FASERν, we propose the detector acts as an instrumented target:

- (i) The bulk of the detector supplies the target mass and is used as a fixed target for the incoming muon flux.
- (ii) Using the precise information about the positions of the muon as it propagates through the detector, the front and rear parts of FASERν are used to measure the incoming and outgoing energies of the muon, respectively, using a method based on multiple Coulomb scattering (MCS), see below.
- (iii) The same spatial information can be used in the bulk of the detector in order to identify the position and magnitude of kinks in the track.

Our track characterization is summarized in a sketch shown in Fig. 1.

A. Muon energy reconstruction

The muon energy reconstruction method relates the observed distribution of scattering angles for a muon traversing the detector to its energy. The method assumes that the dominant source of scattering is multiple Coulomb scattering (MCS) [44–46], a detailed description of the implementation of this method in emulsion detectors can be found in [33,47,48]. In our case, where the depth of a tungsten layer is, $X \sim 1.1$ mm ($X_0^W \approx 3.50$ mm [49]), the typical MCS angle in FASERν for a 100 GeV muon is roughly $\sigma_\theta \sim 0.07$ mrad (the single-layer angular resolution in FASERν is $\sigma_{\mathrm{ang}} \sim 0.23$ mrad, where we used $\sigma_{\mathrm{ang}} = \sqrt{2}\sigma_{\mathrm{pos}}/X$ [33], with $\sigma_{\mathrm{pos}} = 0.18\ \mu$m [50] the spatial resolution of the emulsion plate).

The FASER collaboration reported a momentum reconstruction resolutions of 46% and 57% for 200 GeV and 1 TeV, respectively, applying the MCS method using 100 layers and assuming $\sigma_{\mathrm{pos}} = 0.4\ \mu$m [33]. We analyzed simulated data at lower energies with a more recent resolution estimation ($\sigma_{\mathrm{pos}} = 0.18\ \mu$m), which yielded similar results, for more details see Appendix A. By using a larger sample size of 400 (200 layers of independent x, y displacements), the statistics-dominated energy uncertainty is reduced by about a factor of $\sim\sqrt{400/100} \sim 2$, namely $\Delta E/E \sim 20\%$.

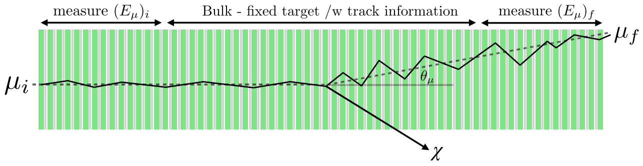

FIG. 1. A sketch of a muon track at FASERν. The initial and final energies can be estimated using the MCS method, where we emphasize using the solid black lines that the MCS angles would generically increase after the muon losses energy. In practice, the MCS angles are $\mathcal{O}(1\ \mathrm{mrad})$ and the muon tracks appear as straight lines (dashed).

An MCS-based method can also be used to determine θ_μ. First, we identify the region in the detector in which the muon lost its energy using a sliding window algorithm. The largest scattering angle measured in this region is strongly correlated with θ_μ, if the scattering angle is larger than the typical MCS angle and is above the angular resolution. This is usually the case for large energy losses, which as we discuss below, is the kinematic region of interest. In a preliminary study, we find that even a simple realization of this algorithm leads to a small reduction in signal efficiency, which can be made even smaller with optimization, e.g., by using machine learning. A detailed study is left for future work.

B. Signal

We calculated the cross section for the coherent process of Eq. (2) (taking N to be tungsten) numerically using MADGRAPH [51] for a range of MFC masses and initial muon energies, see Fig. 2. The cross section depends only weakly on the initial energy of the muon and decreases as expected for heavier MFC masses. Each MFC emission event can be characterized by $\mathcal{R}_{fi}$ and θ_μ. Heavier MFC masses typically lead to larger scattering angles and energy loss, which are strongly correlated, see Fig. 3. Lighter MFC masses, on the other hand, lead to smaller scattering angles and energy loss and are increasingly SM-like. For comparison, we also plot the corresponding distributions from the main background due to bremsstrahlung.

C. Background

The propagation of muons through matter has been studied in detail, see, e.g., [49]. The main SM processes which contribute to the energy loss of the muon as it propagates through matter are, by probability order at small energy losses,

$$N+\mu \to \begin{cases} N+\mu+e^-+e^+ & \text{(Pair production)} \\ N^+ +\mu+e^- & \text{(Ionization)} \\ N+\mu+\gamma & \text{(Bremsstrahlung)} \\ N^* +\mu+\cdots & \text{(Nuclear)} \end{cases}. \qquad (3)$$

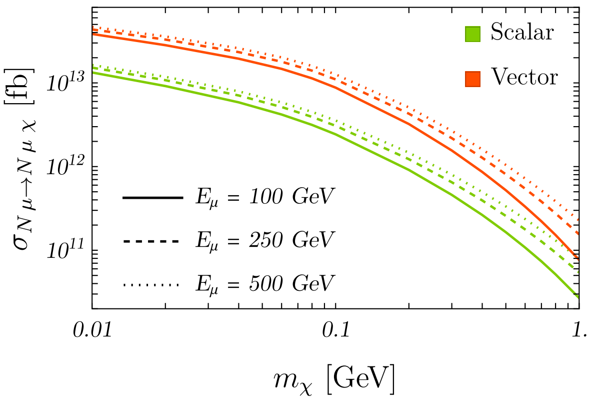

FIG. 2. The $N\mu \to N\mu\chi$ cross-section.

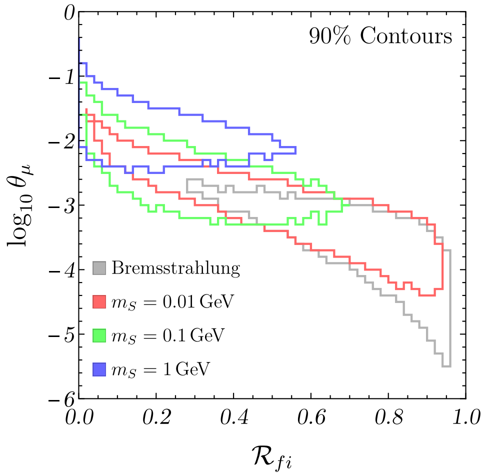

FIG. 3. 90% contour lines of the 2D probability density distribution $\{\mathcal{R}_{fi}, \theta_\mu\}$ for $(E_\mu)_i = 100$ GeV and $\chi = S$ with $m_S = 0.01, 0.1, 1.0$, GeV, plotted in red, green and blue, respectively. For comparison, we plot the same distribution for our dominant background due to bremsstrahlung in gray. The result for $\chi = V$ are very similar, see Appendix C.

As the muon propagates through the tungsten layers, its total energy loss is typically an accumulation of a large number of scatterings due to the processes of Eq. (3). At 100 GeV, the average energy loss in tungsten is $\langle dE/dx \rangle = 3.05\ \mathrm{MeV\,cm^2/gr}$ [49]. Thus, the average energy loss at FASERν would be $\langle \Delta E \rangle \approx 5$ GeV per muon.

The main background source is rare events in which the muon loses a large fraction of its energy due to a SM process. In order to study the background processes, we simulated $\sim 5 \times 10^6$ muon tracks as they propagate through a simplified model of FASERν[1] using GEANT4 [52,53] with various values for the initial energy. We associate each of the simulated tracks with one of the SM processes listed in Eq. (3) according to its single largest energy loss event during its propagation. This identification is useful for tracks in which a rare hard scattering occurred, while tracks with small energy losses are typically a result of many soft scatterings. We present the distribution of tracks and the relevant distributions in Appendix C.

The background (BG) rejection for the three prompt SM processes, i.e., ionization, pair production and nuclear, quantifies the ability to detect energy depositions in the close vicinity of a given muon track. This can be done either by (1) finding a statistically significant excess of secondary particles around the muon track, or by (2) associating an emerging high-energy particle track to the muon track. The transverse length scale of EM showers comprised from secondary particles is given by the Molière radius, $r_\mathrm{M} = 9.3$ mm in tungsten [49]. The other relevant scale is the average inter-track distance $r_\mathrm{track} \sim \rho^{-1/2}$, where ρ is the average track surface density. If $r_\mathrm{track} \gg r_\mathrm{M}$, the

---

[1] The tungsten layers are modeled accurately, but the film is treated as single measurement per film layer.

tracks are sufficiently separated such that each track can be treated in isolation and essentially all SM processes may be easily identified. Using Eq. (6), we estimate

$$\rho \sim \frac{N_\mu}{N_{\rm dev} S} \sim \frac{10^5}{{\rm cm}^2}\left(\frac{20}{N_{\rm dev}}\right)\left(\frac{\mathcal{L}_{\rm LHC}}{250\ {\rm fb}^{-1}}\right), \qquad (4)$$

where $N_{\rm dev}$ is the number of emulsion film development during the run and N_μ/S the number of muons per surface area which depends only the LHC luminosity, see Eq. (6). We find that $r_{\rm track} \sim 0.03$ mm $\ll r_{\rm M}$. Therefore, identifying an excess of secondary particles could be challenging as it would have to be made on top of the pile-up generated by the surrounding tracks. Alternatively, one could try to identify single tracks of high-energy electrons and positrons emerging from a source muon track. These tracks typically emerge at length scales much smaller than the Molière radius and their identification is essentially limited by the spatial resolution of the emulsion track $\sigma_{\rm pos} \ll r_{\rm track}$.

Both approaches outlined above would prove to be more challenging for bremsstrahlung; any sign for the photon emission is expected to be displaced due to the propagation of the photon in matter. The probability of correctly associating a displaced energy deposition with a given track determines the bremsstrahlung BG rejection rate. Beyond the overall ability to detect excess energy deposition anywhere in the detector, the bremsstrahlung rejection rate depends on two additional factors: (1) the typical transverse distance traveled by the photon and (2) the density of relevant tracks, i.e., tracks which could be mistakenly associated with the emitted photon.

The former factor depends on the propagation of photons in FASERν; the mean free path of photons in tungsten is $(9/7)X_0^W \sim 4.5$ mm, and the photon angle distribution peaks around $\theta_\gamma \sim m_\mu/E_\mu \sim 10^{-3}$, see Appendix B for details. Naively, the average transverse displacement is $\sim 4.5 \times 10^{-3}$ mm for a 100 GeV muon, which is an order of magnitude smaller than $r_{\rm track}$. However, photons emitted at larger angles are exponentially more likely to propagate a larger transverse distance, therefore a reliable modeling of the photon angle distribution at large angles is necessary.

The second factor, the tracks density, depends on the kinematic cuts and algorithms used. For example, the number of relevant tracks can be reduced by a factor of $\sim 10^{-2} - 10^{-3}$ by considering only tracks for which a substantial energy loss was observed. The number of relevant tracks can be further reduced by considering only the tracks for which the energy loss occurred in the same region as the track in question. This reduction depends on the efficiency of the algorithm used to identify the energy loss region, such as the sliding window algorithm outlined above. We conclude that a significant fraction of bremsstrahlung events can expected to be vetoed by applying isolation criteria. Further rejection could be achieved by the detection of significant EM deposits (without necessarily requiring a complete photon reconstruction) and the use of kinematic characteristics. The proper development and optimization of this technique requires a detailed experimental study which is beyond the scope of this work.

IV. PROJECTED SENSITIVITY

The expected effective luminosity $\mathcal{L}_{\rm eff}$ per muon on a tungsten target of length Δ is given by

$$\frac{\mathcal{L}_{\rm eff}}{N_\mu} = \frac{\rho_W \Delta}{m_{\rm W}} = \frac{5.1 \times 10^{-15}}{\rm fb}\left(\frac{\Delta}{730 \times 1.1\ {\rm mm}}\right), \qquad (5)$$

where we use $\rho_{\rm W} = 19.3$ gr/cm^3, $m_{\rm W} = 171.35$ GeV [49] and normalize the result to the length of FASERν. The expected number of high-energy muons at FASERν with $E_\mu > 100$ GeV with LHC luminosity $\mathcal{L}_{\rm LHC}$ and detector surface S is [34,35]

$$N_\mu = 2 \times 10^9 \left(\frac{\mathcal{L}_{\rm LHC}}{250\ {\rm fb}^{-1}}\right)\left(\frac{S}{25\ {\rm cm} \times 30\ {\rm cm}}\right), \qquad (6)$$

where we normalize the result to the FASERν surface area and the LHC benchmark luminosity. The expected muon spectrum is dominated by the low energy bins [35]. The energy dependence of the cross sections and relevant kinematic variables on the initial muon energy is small; we find that the inclusion of higher energy bins only generates a small $\mathcal{O}(1\%)$ effect on the projected sensitivity. Thus, for our analysis it is sufficient to assume an incoming beam of 100 GeV muons. The total number of signal events is given by $N_{\rm sig} = \mathcal{L}_{\rm eff} \times \sigma(N\mu \to N\mu\chi)$. The two benchmarks points we consider in this work are for FASERν (FASERν2): $\mathcal{L}_{\rm LHC} = 250$ fb^{-1} (3 ab^{-1}), $S = 25$ cm $\times$ 30 cm (40 cm $\times$ 40 cm) and $\Delta = 730 \times 1.1$ mm (3300×2 mm).

We first consider the optimistic zero-background case, the dot-dashed curves plotted in Fig. 4 in orange (blue) for the FASERν (FASERν2) cases. We learn that FASERν can probe new parameter space at low masses with couplings of $g_{S,V} \sim 10^{-4}$, covering the $(g-2)_\mu$ preferred region, while the reach of FASERν2 increases by more than an order of magnitude.

The number of events expected from the most challenging BG source, bremsstrahlung, is sizeable $B_{\rm brem} \approx 0.07 N_\mu$. Therefore, achieving zero background would require an efficient BG rejection strategy. As a first step, we optimize the kinematic cuts on $\mathcal{R}_{fi}$ and θ_μ for each MFC mass point. For the energy ratio distributions, we assume an energy resolution of 40% from the MCS method. We introduce a signal acceptance factor $\mathcal{A}_{\rm S}^{\rm MCS} = 1 - (200\ {\rm mm})/\Delta$ to account for the fraction of the detector used for initial and final energy measurements. For the θ_μ distribution, we use the angular resolution specified above. We assume the position of θ_μ within the muon track can be identified using a sliding window algorithm utilizing the MCS method.

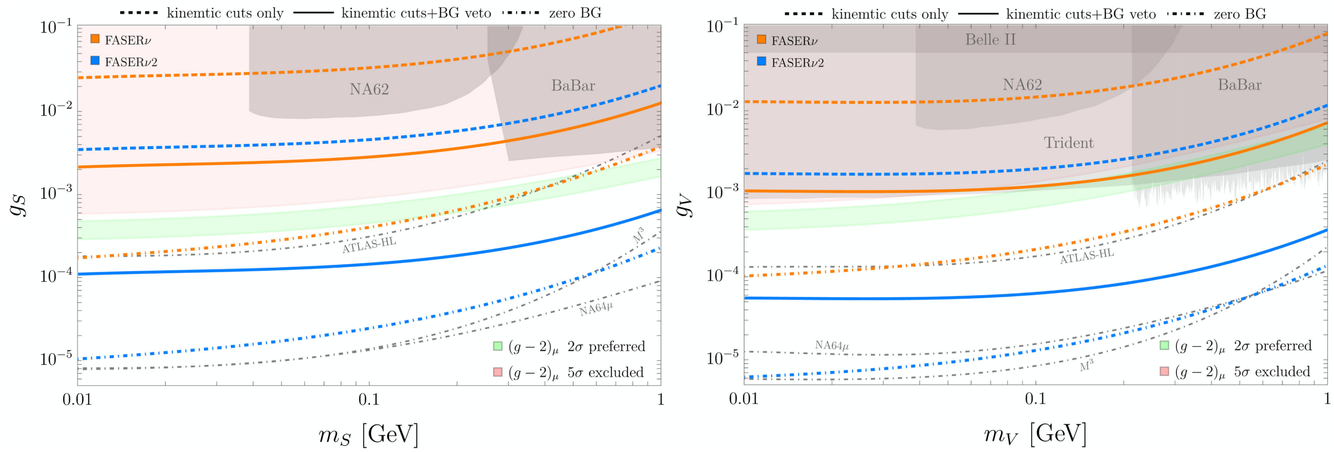

FIG. 4. Projected sensitivity plot for a scalar (left) and vector (right) MFC for FASERν (orange) and FASERν2 (blue), see main text for details. Shaded gray region is ruled out by *BABAR* [4,18] and NA62 [21]. Belle II [19] and trident production [22–24]. The dot-dashed lines are the projected sensitivities from ATLAS-HL [32], M^3 (phase 2) [29] and NA64μ (5×10^{12} muons-on-target) [27].

For light masses, we find the optimal sensitivity by using looser cuts, $\theta_\mu \gtrsim 1$ mrad and $\mathcal{R}_{fi} \lesssim 0.5(0.7)$ for vector (scalar) MFC, which reduce the main BG sources, bremsstrahlung and ionization, with the respective BG rejections $\epsilon^{\text{kin.}}_{\text{brem}} \sim 0.07$ and $\epsilon^{\text{kin.}}_{\text{ion}} \sim 0.01$, while still allowing a reasonable signal efficiency $\epsilon^{\text{kin.}}_{\text{S}} \sim 0.2$. For heavy masses, applying tighter cuts, $\theta_\mu \gtrsim 10$ mrad and $\mathcal{R}_{fi} \lesssim 0.25(0.7)$ for vector (scalar) MFC, strongly suppresses the BG due to ionization, leaving mostly bremsstrahlung events with $\epsilon^{\text{kin.}}_{\text{brem}} \sim 0.01$, while minimally effecting the signal sensitivity which actually increases $\epsilon^{\text{kin.}}_{\text{S}} \sim 0.8$ due to the shift of the signal to higher scattering angles and larger energy losses. The resulting sensitivities using the above-mentioned kinematic cuts are plotted in Fig. 4. This is the worst-case scenario, where the BG events are not vetoed, leaving much room for improvement.

The solid curves in Fig. 4 represent the more realistic scenario in which some of the background events that survive the kinematic cuts are vetoed due to the detection of the deposited energy in the detector. We estimate a bremsstrahlung rejection rate of $\epsilon^{\text{veto}}_{\text{brem}} = 5 \times 10^{-5} (10^{-6})$ for the FASERν (FASERν2) benchmark. This estimation is based on the exponential decay rate of photons, their angular distribution and taking into account the relevant density of tracks around a track under consideration. While we expect higher rejection rates for the remaining BG processes, we conservatively apply the same rejection rate to all BG types.

V. OUTLOOK

In this work, we propose to utilize FASERν as a muon fixed target experiment to search for new muon force carriers (MFCs), taking advantage of the large muons flux of $\sim 10^9/250\ \text{fb}^{-1}$. In addition to its role as a fixed target, the emulsion detector measures the muon track with excellent spatial resolution. This information can be used to measure kinks in the track, as well as the incoming and outgoing muon energies based on multiple coulomb scattering. Tracks with missing energy and large kinks are prime signatures of MFCs. We find that FASERν will potentially probe previously unexplored regions of the MFC parameter space within the current run. Future runs will have substantially increased sensitivity and can be competitive with dedicated MFC searches such as M^3 and NA64$_\mu$.

This study should be considered as a proof of concept. Reaching the full potential of FASERν would therefore require additional dedicated studies to develop and optimize various techniques, e.g., a rejection algorithm for the bremsstrahlung background events. Moreover, we did not include directional information, available due to the finite width of the emulsion layers, which can potentially improve the analysis. Another interesting possibility would be to use rare SM processes such as muon trident production in FASERν as probe of vector MFCs. Interestingly, a larger muon flux is expected to be found only a few meters away from the current location of FASER. A well-placed dedicated muon detector could then potentially reach sensitivities well beyond the existing bounds and future dedicated searches. Finally, the above method can be implemented in other emulsion detectros at the LHC, e.g., SND@LHC.

ACKNOWLEDGMENTS

We thank Jamie Boyd and Jonathan Feng for comments on the manuscript. A. A. is supported by the European Research Council (ERC) under the European Union's Horizon 2020 research and innovation programme (Grant agreement No. 101002690) and JSPS KAKENHI Grant No. JP20K23373. R. B. and Y. S. are supported by grants from the NSF-BSF (No. 2021800), the ISF (No. 483/20), the BSF (No. 2020300) and by the Azrieli foundation. I. G. is supported by grant from ISF (No. 751/19). E. K. is supportted by grants from NSF-BSF (No. 2020785) and the ISF (No. 1638/18 and 2323/18).

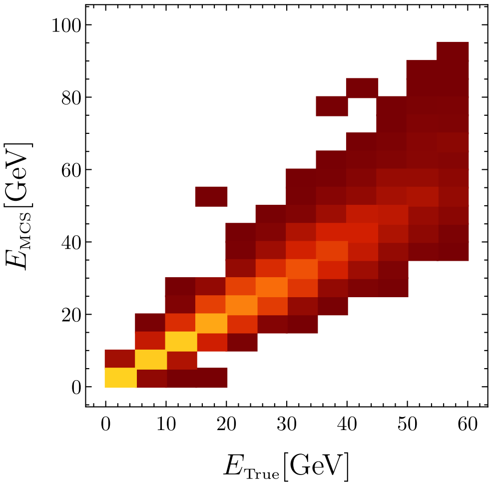

FIG. 5. Density distribution of E_{MCS}, the measured energy using the MCS method, and the true energy E_{True}.

APPENDIX A: ENERGY MEASUREMENT ANALYSIS

We performed an analysis of the energy measurement using the MCS method at lower energies < 100 GeV from $\mathcal{O}(10^3)$ simulated tracks. From each track, we used 200 shifts in both the x and y directions to estimate the energy of the muon using the MCS method outline in the main text. We plot the result of our analysis in Fig. 5. We find that the absolute resolution increases at lower energies due to the larger shifts compared to the spatial resolution. The relative resolution is approximately constant at ≈20%, with the exception of lower energies. See Table 1 for a summary of our results.

APPENDIX B: BREMSSTRAHLUNG IN FASERν

High-energy photons ($\gtrsim 100$ MeV) are typically converted into an e^+e^- pair in the nuclear electromagnetic field. The mean free path of the photon is given by $(9/7)X_0$, with X_0 the radiation length of the relevant material. The physical propagation distance of a high-energy photon produced inside FASERν, which we denote by X_γ, is distributed according to an exponential distribution

$$\Delta_\gamma \sim \exp\left[-\frac{1}{(9/7)X_0^W}\left(\frac{\Delta_{\mathrm{W}}}{\Delta_{\mathrm{W}}+\Delta_{\mathrm{emu.}}}\right)X_\gamma\right], \qquad \text{(B1)}$$

where $\Delta_{\mathrm{W}} = 1.1\mathrm{mm}$ and $\Delta_{\mathrm{emu.}} = 0.34\mathrm{mm}$ are the widths of the tungsten and film layers, respectively. In addition to the propagation distance, we expect the photon angle distribution emitted from high-energy muons to be peaked around

$$\theta_\gamma \sim \frac{m_\mu}{E_\mu}. \qquad \text{(B2)}$$

TABLE I. A summary of energy measurement using the MCS method described in the text. At lower energy, larger scattering angles allow for a better (absolute) energy resolution, while the relative resolution is relatively fixed at around 20% for all energies, with the exception of the first energy bin.

$[E_{\mathrm{min}}, E_{\mathrm{max}}]$ [GeV]	# of tracks	$\langle E\rangle$ [GeV]	σ_E [GeV]	$\sigma_E/\langle E\rangle$
[0,10]	1028	5.63	3.13	55.6%
[10,20]	1264	15.87	4.24	26.7%
[20,30]	1214	25.8	5.36	20.8%
[30,40]	1060	35.76	6.84	19.1%
[40,50]	726	45.28	8.4	18.5%
[50,60]	400	56.65	10.54	18.6%
[99.9,100.1]	3557	102.75	18.78	18.3%

TABLE II. Distribution of tracks according to the SM process responsible for the largest energy loss along the track. This distribution was calculated for initial muon energy of 100 GeV. Note that at these high energies, the dependence of these rates on the initial muon energy is negligible.

	Pair	Ionization	Brems.	Nuclear	Total
# of tracks	3.15×10^6	1.42×10^6	3.45×10^5	4.7×10^4	4.96×10^6
Fraction	0.63	0.29	0.07	0.009	1.0

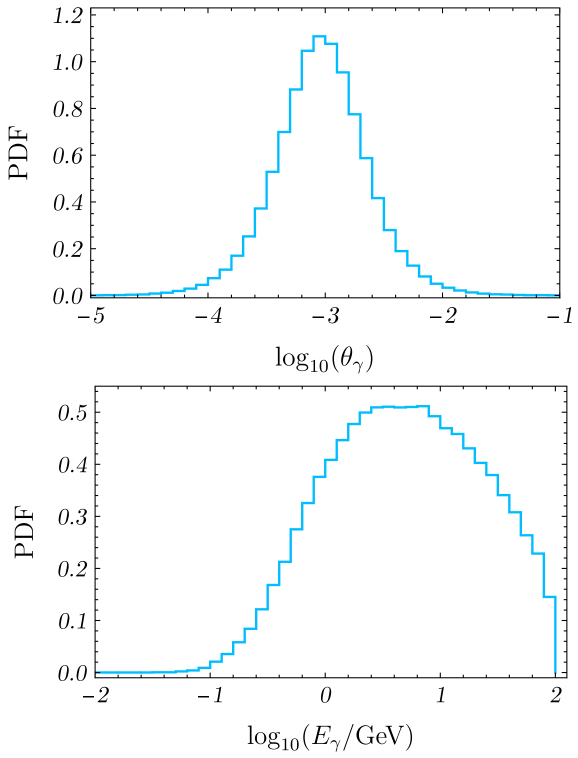

FIG. 6. Left: probability distribution for the emitted photon angle θ_γ. Right: probability distribution of the emitted photon energy E_γ.

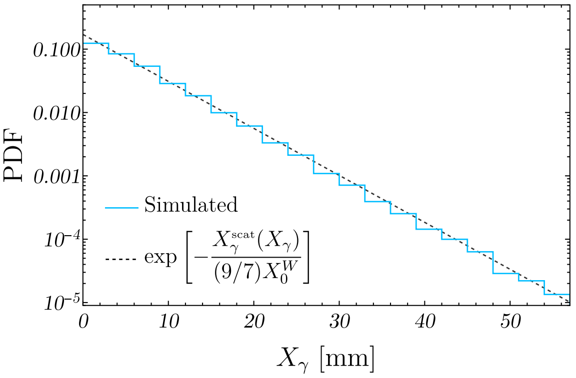

FIG. 7. Probability distribution of the physical propagation distance of the photon X_γ as calculated bu simulation (solid blue) compared to the analytic expectation of Eq. (B1) (dashed black).

This can be easily seen by examining the bremsstrahlung differential cross section [54], where terms of the form $\sin^2\theta/(E-|p|\cos\theta)^2$ are maximized for $\cos\theta = \frac{p}{E}$. After taking the small-angle and high-energy limits, one recovers Eq. (B2).

To validate Eqs. (B1) and (B2), we studied $\approx 3\times 10^5$ simulated muon tracks associated with a hard photon emission (see Table 2) and extracted the photon information. In Fig. 6, we show the angular (left panel) and energy (right panel) distribution of the emitted photons. As expected, the angular distribution is strongly peaked around $m_\mu/E_\mu \sim 10^{-3}$, consistent with the simulated data used with a constant initial muon energy of $E_\mu = 100$ GeV. The energy distribution is relatively flat at its bulk region, with the expected threshold at 100 GeV (the maximal available energy) and a tail for the low-energy photons. At shown in Fig. 10, at low energy losses, the bremsstrahlung rate is suppressed, and therefore it is not likely that a soft $\mathcal{O}(1)$ GeV photon is responsible for the largest energy loss in a given track, which qualitatively explains the fast-dropping tail at low photon energies in Fig. 6. In Fig. 7 we show the simulated distribution of X_γ, where we find a good agreement with the theoretical prediction of Eq. (B1).

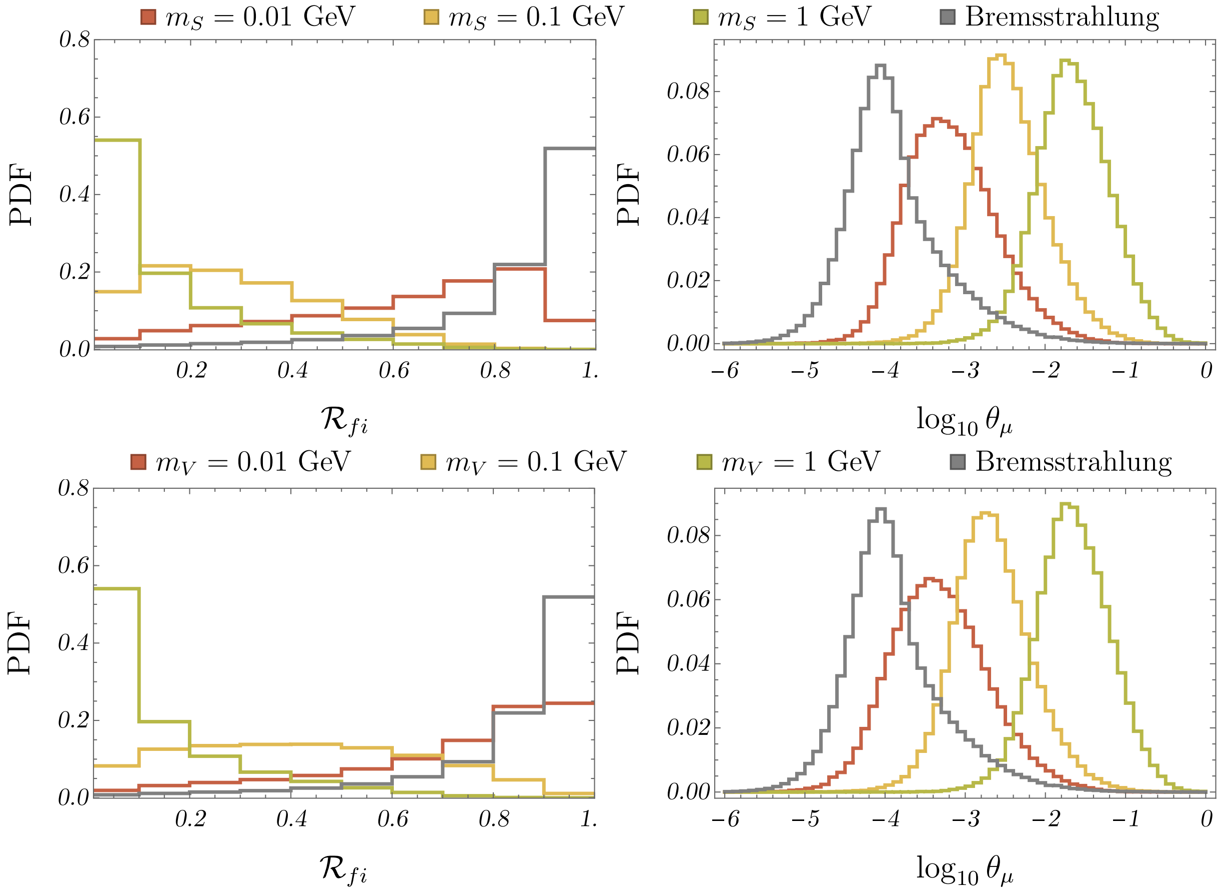

FIG. 8. Signal $\mathcal{R}_{fi}$ and θ_μ distributions for $(E_\mu)_i = 100$ GeV and three representative scalar (top) and vector (bottom) MFC masses, 0.01 GeV, 0.1 GeV, and 1 GeV in red, yellow, and green, respectively. For comparison, we plot the same distribution for our dominant background due to bremsstrahlung.

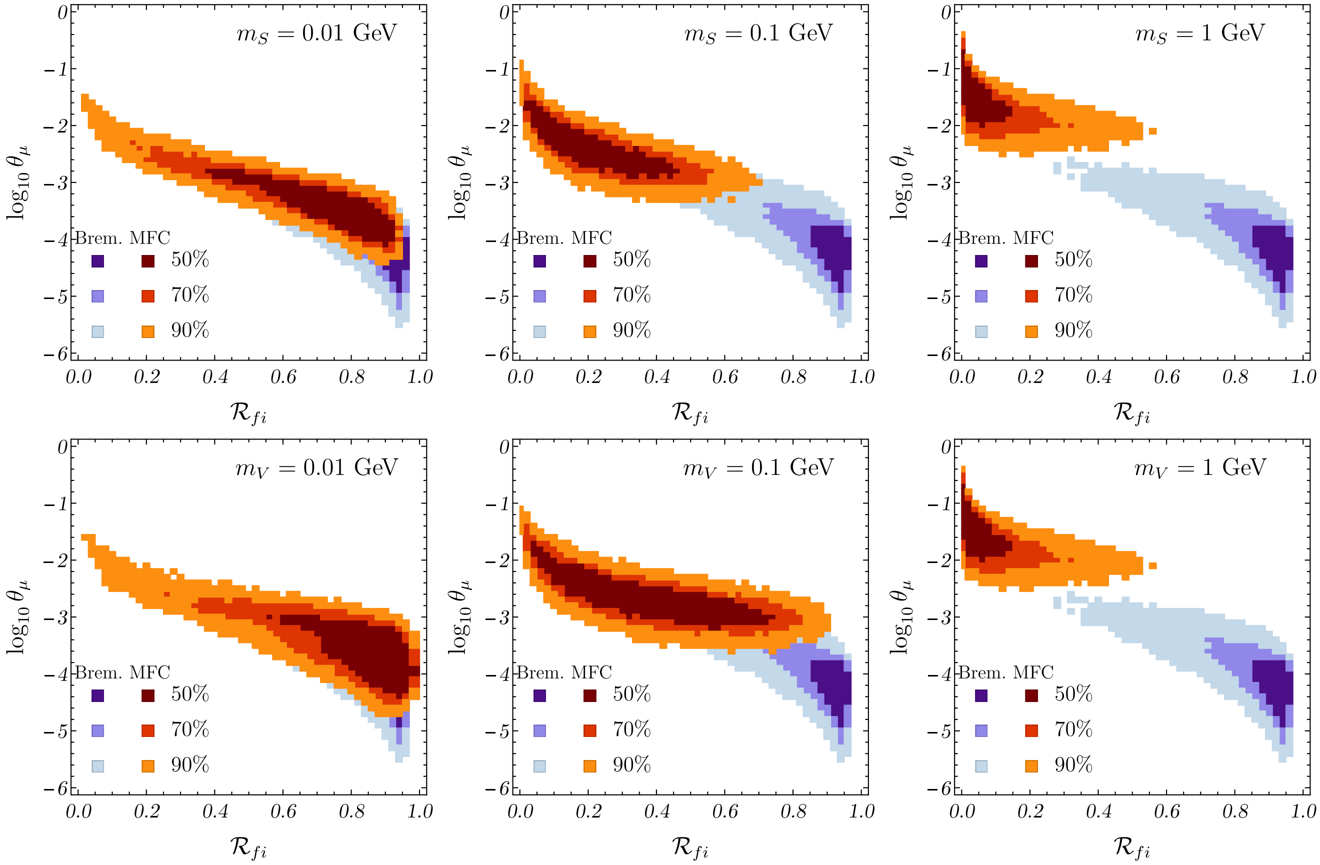

FIG. 9. 2D probability density distribution $\{\mathcal{R}_{fi}, \theta_\mu\}$ for $(E_\mu)_i = 100$ GeV and three representative scalar (top) and vector (bottom) MFC masses, 0.01 GeV (left), 0.1 GeV (center), and 1 GeV (right). For comparison, we plot the same distribution for our dominant background due to bremsstrahlung.

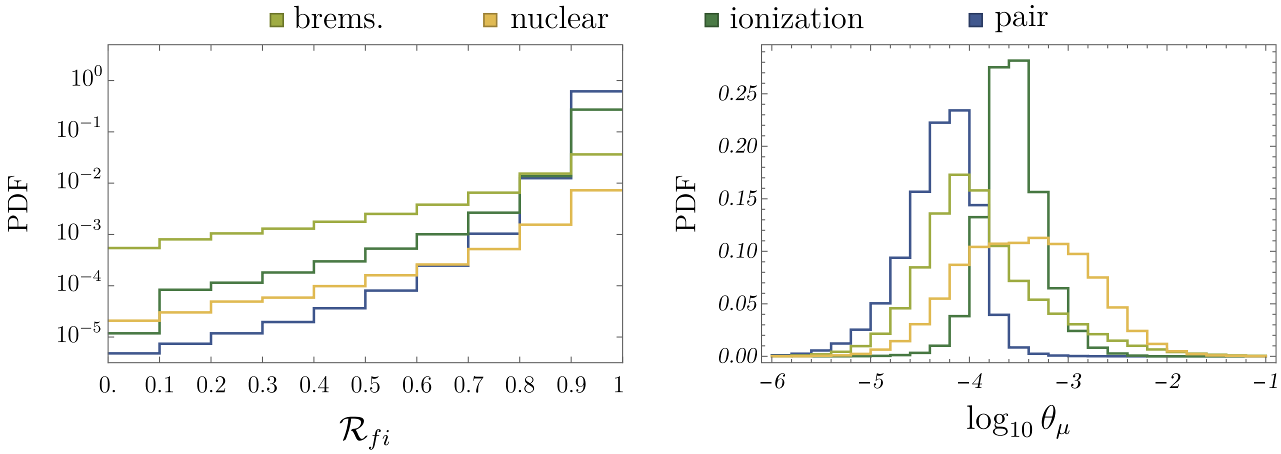

FIG. 10. Background $\mathcal{R}_{fi}$ (left) and θ_μ (right) distributions for bremsstrahlung (light green), nuclear (yellow), ionization (dark green) and pair production (blue) processes of Eq. (3) with $(E_\mu)_i = 100$ GeV. Note that the $\mathcal{R}_{fi}$ distributions are weighted according to the values in Table 2, such that the sum of all four curves is normalized to 1.

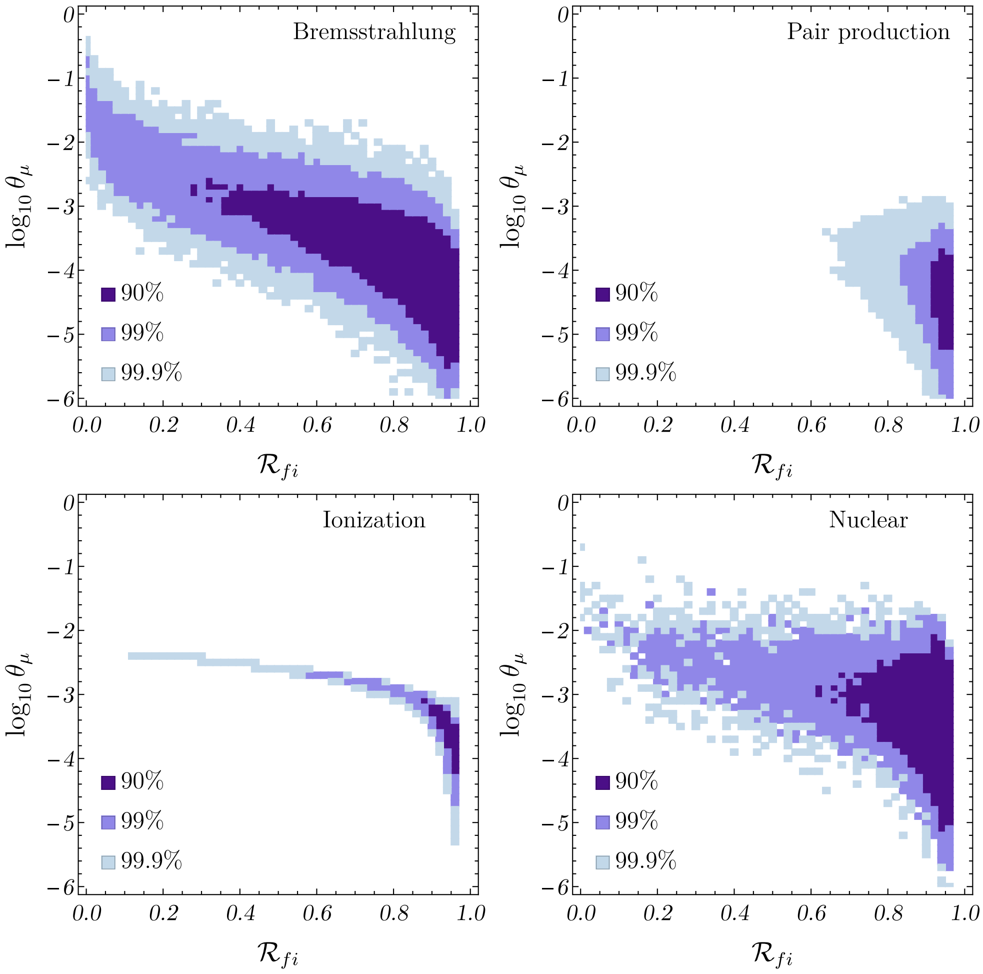

FIG. 11. 2D probability density distribution $\{\mathcal{R}_{fi}, \theta_\mu\}$ for bremsstrahlung, nuclear, ionization and pair production process shown in the main text with $(E_\mu)_i = 100$ GeV.

APPENDIX C: KINEMATICAL PROPERTIES OF THE SIGNAL AND BACKGROUNDS

Here we explore the different energy losses, R_{fi} and scattering angle, θ_μ of the signal and backgrounds. The MFC and the dominant background, bremsstrahlung, $\mathcal{R}_{fi}$ and θ_μ distributions are plotted in Fig. 8. In Fig. 9, we show the $\mathcal{R}_{fi}$ vs θ_μ signal and background distributions for several MFC masses. The $\mathcal{R}_{fi}$ and θ_μ probability distributions for each individual background and signal processes are plotted in Fig. 10. Table 2 contains the fraction of events of each process. The correlation between the kinematic variables can be seen in the density plots of Fig. 11. As expected, the vast majority of these scattering events generate small energy loss, $\Delta E \lesssim \langle \Delta E \rangle$, while the rare large energy loss events are dominated by bremsstrahlung. Finally, Table 3 summaries the kinematics cuts, the signal efficiency and remaining backgrounds.

TABLE III. Kinematics cuts, signal efficiency $\epsilon_S^{\rm kin}$ and remaining background count for the four SM processes for our FASERν benchmark at the edges of the considered mass region. The cuts at intermediate mass points were chosen to optimize sensitivity.

	$\mathcal{R}_{fi}$	θ_μ	$\epsilon_S^{\rm kin}$	$N_{\rm BG,brem}$	$N_{\rm BG,ion}$	$N_{\rm BG,pair}$	$N_{\rm BG,nuc}$
$m_S = 0.01$ GeV	$\lesssim 0.7$	$\gtrsim 1$ mrad	~ 0.2	9.9×10^6	8.9×10^6	2.5×10^5	2.0×10^6
$m_S = 1$ GeV	$\lesssim 0.7$	$\gtrsim 10$ mrad	~ 0.8	1.4×10^6	4.3×10^3	1.1×10^4	1.3×10^5
$m_V = 0.01$ GeV	$\lesssim 0.5$	$\gtrsim 1$ mrad	~ 0.2	8.5×10^6	5.7×10^6	1.7×10^5	1.4×10^6
$m_V = 1$ GeV	$\lesssim 0.25$	$\gtrsim 10$ mrad	~ 0.8	1.1×10^6	4.3×10^3	6.6×10^3	1.3×10^5

[1] R. K. Ellis *et al.*, Physics briefing book: Input for the European strategy for particle physics update 2020, arXiv:1910.11775.

[2] P. Agrawal *et al.*, Feebly-interacting particles: FIPs 2020 workshop report, Eur. Phys. J. C **81**, 1015 (2021).

[3] G. Lanfranchi, M. Pospelov, and P. Schuster, The search for feebly interacting particles, Annu. Rev. Nucl. Part. Sci. **71**, 279 (2021).

[4] B. Batell, N. Lange, D. McKeen, M. Pospelov, and A. Ritz, Muon anomalous magnetic moment through the leptonic Higgs portal, Phys. Rev. D **95**, 075003 (2017).

[5] C.-Y. Chen, M. Pospelov, and Y.-M. Zhong, Muon beam experiments to probe the dark sector, Phys. Rev. D **95**, 115005 (2017).

[6] B. Batell, A. Freitas, A. Ismail, and D. Mckeen, Flavor-specific scalar mediators, Phys. Rev. D **98**, 055026 (2018).

[7] L. Marsicano, M. Battaglieri, A. Celentano, R. De Vita, and Y.-M. Zhong, Probing leptophilic dark sectors at electron beam-dump facilities, Phys. Rev. D **98**, 115022 (2018).

[8] G. W. Bennett *et al.*, Final report of the E821 muon anomalous magnetic moment measurement at BNL, Phys. Rev. D **73**, 072003 (2006).

[9] Muon g-2 Collaboration, Measurement of the positive muon anomalous magnetic moment to 0.46 ppm, Phys. Rev. Lett. **126**, 141801 (2021).

[10] Muon g-2 Collaboration, Measurement of the positive muon anomalous magnetic moment to 0.20 ppm, Phys. Rev. Lett. **131**, 161802 (2023).

[11] M. Pospelov, Secluded U(1) below the weak scale, Phys. Rev. D **80**, 095002 (2009).

[12] F. Jegerlehner and A. Nyffeler, The Muon g-2, Phys. Rep. **477**, 1 (2009).

[13] S. Borsanyi *et al.*, Leading hadronic contribution to the muon magnetic moment from lattice QCD, Nature (London) **593**, 51 (2021).

[14] C. Alexandrou *et al.*, Lattice calculation of the short and intermediate time-distance hadronic vacuum polarization contributions to the muon magnetic moment using twisted-mass fermions, Phys. Rev. D **107**, 074506 (2023).

[15] M. Cè *et al.*, Window observable for the hadronic vacuum polarization contribution to the muon $g-2$ from lattice QCD, Phys. Rev. D **106**, 114502 (2022).

[16] CMD-3 Collaboration, Measurement of the $e^+e^- \to \pi^+\pi^-$ cross section from threshold to 1.2 GeV with the CMD-3 detector, arXiv:2302.08834.

[17] R. Balkin, C. Delaunay, M. Geller, E. Kajomovitz, G. Perez, Y. Shpilman, and Y. Soreq, Custodial symmetry for muon g-2, Phys. Rev. D **104**, 053009 (2021).

[18] *BABAR* Collaboration, Search for a muonic dark force at *BABAR*, Phys. Rev. D **94**, 011102 (2016).

[19] Belle-II Collaboration, Search for an invisibly decaying Z' boson at Belle II in $e^+e^- \to \mu^+\mu^-(e^\pm\mu^\mp)$ plus missing energy final states, Phys. Rev. Lett. **124**, 141801 (2020).

[20] G. Krnjaic, G. Marques-Tavares, D. Redigolo, and K. Tobioka, Probing muonphilic force carriers and dark matter at kaon factories, Phys. Rev. Lett. **124**, 041802 (2020).

[21] NA62 Collaboration, Search for K^+ decays to a muon and invisible particles, Phys. Lett. B **816**, 136259 (2021).

[22] CHARM-II Collaboration, First observation of neutrino trident production, Phys. Lett. B **245**, 271 (1990).

[23] CCFR Collaboration, Neutrino tridents and W Z interference, Phys. Rev. Lett. **66**, 3117 (1991).

[24] W. Altmannshofer, S. Gori, M. Pospelov, and I. Yavin, Neutrino trident production: A powerful probe of new physics with neutrino beams, Phys. Rev. Lett. **113**, 091801 (2014).

[25] D. Croon, G. Elor, R. K. Leane, and S. D. McDermott, Supernova muons: New constraints on Z' bosons, axions and ALPs, J. High Energy Phys. 01 (2021) 107.

[26] A. Caputo, G. Raffelt, and E. Vitagliano, Muonic boson limits: Supernova redux, Phys. Rev. D **105**, 035022 (2022).

[27] C.-Y. Chen, J. Kozaczuk, and Y.-M. Zhong, Exploring leptophilic dark matter with NA64-μ, J. High Energy Phys. 10 (2018) 154.

[28] S. N. Gninenko, D. V. Kirpichnikov, M. M. Kirsanov, and N. V. Krasnikov, Combined search for light dark matter with electron and muon beams at NA64, Phys. Lett. B **796**, 117 (2019).

[29] Y. Kahn, G. Krnjaic, N. Tran, and A. Whitbeck, M^3: A new muon missing momentum experiment to probe $(g-2)_\mu$ and dark matter at Fermilab, J. High Energy Phys. 09 (2018) 153.

[30] D. Forbes, C. Herwig, Y. Kahn, G. Krnjaic, C. M. Suarez, N. Tran, and A. Whitbeck, New searches for muonphilic particles at proton beam dump spectrometers, Phys. Rev. D **107**, 116026 (2023).

[31] C. Cesarotti, S. Homiller, R. K. Mishra, and M. Reece, Probing new gauge forces with a high-energy muon beam dump, Phys. Rev. Lett. **130**, 071803 (2023).

[32] I. Galon, E. Kajamovitz, D. Shih, Y. Soreq, and S. Tarem, Searching for muonic forces with the ATLAS detector, Phys. Rev. D **101**, 011701 (2020).

[33] FASER Collaboration, Detecting and studying high-energy collider neutrinos with FASER at the LHC, Eur. Phys. J. C **80**, 61 (2020).

[34] FASER Collaboration, Technical proposal: FASERnu, arXiv:2001.03073.

[35] FASER Collaboration, First neutrino interaction candidates at the LHC, Phys. Rev. D **104**, L091101 (2021).

[36] J. L. Feng, I. Galon, F. Kling, and S. Trojanowski, ForwArd search experiment at the LHC, Phys. Rev. D **97**, 035001 (2018).

[37] FASER Collaboration, Letter of intent for FASER: Forward search experiment at the LHC, arXiv:1811.10243.

[38] FASER Collaboration, Technical proposal for FASER: Forward search experiment at the LHC, arXiv:1812.09139.

[39] FASER Collaboration, FASER's physics reach for long-lived particles, Phys. Rev. D **99**, 095011 (2019).

[40] X. G. He, G. C. Joshi, H. Lew, and R. R. Volkas, New Z-prime phenomenology, Phys. Rev. D **43**, 22 (1991).

[41] R. Foot, New physics from electric charge quantization?, Mod. Phys. Lett. A **06**, 527 (1991).

[42] X.-G. He, G. C. Joshi, H. Lew, and R. R. Volkas, Simplest Z' model, Phys. Rev. D **44**, 2118 (1991).

[43] FASER Collaboration, First direct observation of collider neutrinos with FASER at the LHC, Phys. Rev. Lett. **131**, 031801 (2023).

[44] H. A. Bethe, Moliere's theory of multiple scattering, Phys. Rev. **89**, 1256 (1953).

[45] W. T. Scott, The theory of small-angle multiple scattering of fast charged particles, Rev. Mod. Phys. **35**, 231 (1963).

[46] J. W. Motz, H. Olsen, and H. W. Koch, Electron scattering without atomic or nuclear excitation, Rev. Mod. Phys. **36**, 881 (1964).

[47] K. Kodama *et al.*, Detection and analysis of tau neutrino interactions in DONUT emulsion target, Nucl. Instrum. Methods Phys. Res., Sect. A **493**, 45 (2002).

[48] OPERA Collaboration, Momentum measurement by the multiple coulomb scattering method in the OPERA lead emulsion target, New J. Phys. **14**, 013026 (2012).

[49] Particle Data Group, Review of particle physics, Prog. Theor. Exp. Phys. **2022**, 083C01 (2022).

[50] H. Kawahara, FASERnu: Current status and first data from LHC run 3, http://indico.cern.ch/event/1166678/contributions/5082108/ (2022).

[51] J. Alwall, R. Frederix, S. Frixione, V. Hirschi, F. Maltoni, O. Mattelaer, H.-S. Shao, T. Stelzer, P. Torrielli, and M. Zaro, The automated computation of tree-level and next-to-leading order differential cross sections, and their matching to parton shower simulations, J. High Energy Phys. 07 (2014) 079.

[52] GEANT4 Collaboration, GEANT4–a simulation toolkit, Nucl. Instrum. Methods Phys. Res., Sect. A **506**, 250 (2003).

[53] A. G. Bogdanov, H. Burkhardt, V. N. Ivanchenko, S. R. Kelner, R. P. Kokoulin, M. Maire, A. M. Rybin, and L. Urban, GEANT4 simulation of production and interaction of muons, IEEE Trans. Nucl. Sci. **53**, 513 (2006).

[54] H. Bethe and W. Heitler, On the stopping of fast particles and on the creation of positive electrons, Proc. R. Soc. A **146**, 83 (1934).